STA-20: An ABC-6 Zeotype Structure Prepared by Co-Templating and Solved via a Hypothetical Structure Database and STEM-ADF Imaging

Alessandro Turrina,[*,1,2] Raquel Garcia,[2] Abigail E. Watts,[1] Heather F. Greer,[1] Jonathan Bradley,[3] Wuzong Zhou,[1] Paul A. Cox,[4] Mervyn D. Shannon,[2] Alvaro Mayoral,[5] John L. Casci[2] and Paul A. Wright[*,1]

[1] *EaStCHEM School of Chemistry, University of St Andrews, Purdie Building, North Haugh, St Andrews, KY16 9ST, United Kingdom.*

[2] *Johnson Matthey Technology Centre, Chilton PO Box 1, Belasis Avenue, Billingham, TS23 1LB, United Kingdom.*

[3] *Johnson Matthey Technology Centre, Blount's Court, Sonning Common, Reading, RG4 9NH, United Kingdom.*

[4] *School of Pharmacy and Biomedical Sciences, University of Portsmouth, St. Michael's Building, White Swan Road, Portsmouth, PO1 2DT, United Kingdom.*

[5] *Laboratorio de Microscopias Avanzadas (LMA), Instituto de Nanociencia de Aragon (INA), Universidad de Zaragoza, Mariano Esquillor, 50018 Zaragoza, Spain.*

* Corresponding Authors. E-mail: alessandro.turrina@matthey.com; paw2@st-andrews.ac.uk

Abstract

A microporous silicoaluminophosphate with a novel topology type, STA-20, has been prepared via a dual templating method using hexamethylene bisdiazabicyclooctane (diDABCO-C6) and trimethylamine as co-templates. Its structure has been solved and

confirmed using a multi-technique approach that included the use of a hypothetical zeolite database to obtain a candidate starting structure, followed by scanning transmission electron microscopy with annular dark field imaging and Rietveld refinement. STA-20 is a member of the ABC-6 family of zeotype structures. The structure has trigonal symmetry, P-31c, with a = 13.15497(18) Å and c = 30.5833(4) Å in the calcined form. It has a 12-layer stacking sequence of 6-rings (6Rs), AABAABAACAAC(A), which contains single and double 6R units. As well as $d6r$, can and gme cages, STA-20 possesses the longest cage observed in an ordered ABC-6 material, giving a 3D-connected pore system limited by 8R windows. Models for the location of the templates within cages of the framework were obtained by combining elemental analysis, ^{13}C MAS NMR, computer modelling and Rietveld refinement.

Introduction

Small pore aluminosilicate zeolites and their silicoaluminophosphate (SAPO) zeotype analogues[1] have in recent years found widespread application in catalytic processes, the most important of which are the generation of light olefins from methanol over their acid forms via acid catalysis (the MTO reaction)[2-6] and the reduction of NOx emissions from lean burn engines via selective catalytic reduction with ammonia over their copper forms.[7-12] In particular, structures with pore space comprising cavities connected three-dimensionally via rings of eight tetrahedral cations and eight oxygen atoms (8Rs) are suitable for these reactions. These include many structures drawn from the so-called ABC-6 family of polytypes,[14-16] which are built up from layers of 6Rs, linked by 4Rs, with different stacking sequences. The 6R units can be centred on three different (x, y) positions in the hexagonal ab-plane: A (0, 0), B (2/3, 1/3) and C (1/3, 2/3) and stacking sequences include double 6-ring units (D6Rs) as well as 6Rs. Materials representing 22 such polytypes of the ABC-6 family

have been reported, each with its own characteristic stacking sequence. The CHA framework topology, for example (each distinct topology is given a three letter code), may be prepared in aluminosilicate form (synthetic chabazites, including the high Si/Al SSZ-13[17]) as well as with silicoaluminophosphate composition, SAPO-34.[18] Both find widespread catalytic application.[4,6-13] In these and in many other ABC-6 structures, cages of cross-sectional diameter of ca. 7 Å are linked three dimensionally via elliptical 8Rs, which have minimum openings of around 3.4 Å (small pore). Other well studied examples of synthetic ABC-6 type materials include those with the topology types LEV (zeolite levynite, SAPO-35), ERI (zeolite ZSM-34; SAPO-17) and AFX (zeolite SSZ-16, SAPO-56).[14]

New ABC-6 type materials continue to be discovered, both as zeolites and aluminophosphates, particularly due to the innovative use of organic structure directing agents (OSDAs) that act to template specific cages during crystallisation due to favourable short range non-bonding interactions.[19-24] Xie et al. recently reported the structure of the zeolite SSZ-52, with a structure based on a 18-layer stacking repeat,[25,26] Broach et al. reported two zincoaluminophosphates with novel stacking sequences[27] and Li et al. reported two new ABC-6 magnesioaluminophosphates.[16] Furthermore, topological consideration and molecular modelling indicates that many stacking sequences are possible for which no corresponding materials have been observed, even though they are energetically feasible. Li et al have recently enumerated the 84,292 hypothetical structures in this ABC-6 family with repeat units up to 16 layers and identified by modelling the 1,127 of these that are most likely to be feasible.[16]

One feature of the more complex of these structures is that they contain more than one cage type, and so may be targets for a 'co-templating' approach, where two organic structure directing agents (OSDAs) are incorporated simultaneously during crystallisation, each templating a specific cage type.[28,29] Recently, we have had success in using a co-templating

approach, making use of computational modelling, to prepare SAPOs in the ABC-6 system. In this 'retrosynthetic' method, trimethylamine was found to be effective as a template for *gme* cages and longer bis diazabicyclooctane alkane cations were found to act as templates for the elongated *aft* and *sfw cages*.[30] In this way the ABC-6 small pore SAPOs SAPO-56 and SAPO (SFW) were successfully prepared, the latter for the first time, and with a very high degree of crystallinity.

Here we report the synthesis of a SAPO in the ABC-6 system with a novel topology type, denoted STA-20 (St. Andrews microporous material-20), using the co-templating approach. This was first identified as an impurity in the dual-template synthesis of SAPO STA-18 (SFW),[30] and it has been prepared phase pure by careful optimisation of the synthetic conditions. Its structure is well ordered, but it is prepared in microcrystalline form, precluding structure solution by single crystal X-ray diffraction. Nevertheless, it was possible to determine the unit cell dimensions by selected area electron diffraction and use a hypothetical zeolite structure database to obtain a plausible structural model, which was confirmed by spherical aberration corrected (C_s-corrected) scanning transmission electron microscope (STEM) imaging of unprecedented resolution for a SAPO and refined successfully against synchrotron X-ray powder diffraction data.

Experimental details

Synthesis and preparation

During the experimental investigation, synthesis gels were prepared by mixing orthophosphoric acid (85 wt.% in H_2O, BDH) with silica (either colloidal, 30 wt.% in H_2O, PX-30 or fumed, powder 0.007 μm Aldrich or Cabosil M5, Cabot, >99.8), aluminium

hydroxide (Aldrich or Alfa Aesar), diDABCO-C6 (99%, Alfa Aesar) and trimethylamine, TrMA, (45 wt.% in H_2O, Aldrich) in water and stirred at room temperature. Tetrabutylammonium hydroxide, TBAOH, (40 wt.% in H_2O, Aldrich, or 55 wt.% in H_2O, Sachem) was used to adjust the gel pH to 7. In order to favour the crystallisation of the desired phase, seeds of SAPO AFX, previously prepared (2.0 - 4.0 wt.% with respect to SiO_2 content) were added and the gels heated isothermally at 160 or 190 ºC.

In the final optimized synthesis of STA-20, the overall gel composition was $Al(OH)_3$: 0.9 H_3PO_4 : 0.1 SiO_2 : 0.1 $(diDABCO\text{-}C6)Br_2$: 0.42 TrMA : 0.08 TBAOH : 40 H_2O with 2.0 wt. % of AFX seeds, using fumed Cabosil silica, aluminium hydroxide from Alfa Aesar and TBAOH from Sachem. The final gel was stirred continuously for 2 h at room temperature until homogeneous and then transferred to a Teflon-lined stainless steel autoclave. It was heated under rotation (30 rpm) at 160 °C for 24 h. The resultant product was collected by centrifugation, washed with deionised H_2O and dried overnight at 110 °C.

Characterisation

For phase identification purposes, X-ray powder patterns in the 2θ range 5 - 50° (step size 0.01°, time step 160 s, 0.04 rad Soller, 45 kV, 35 mA) were recorded either on a PANalytical Empyrean automated diffractometer equipped with a X'Celerator detector (Bragg-Brentano geometry, Cu Kα$_1$ X-radiation, λ = 1.54056 Å, via a primary monochromator) or using a Bruker D8 Advance fitted with a copper anode (Cu Kα$_1$) and a LynxEye detector (primary beam fitted with a Göbel mirror with a measurement circle of 280 mm, a slit of 0.22 mm and an axial Soller of 2.5 °; secondary beam with a measurement circle of 280 mm and axial Soller of 2.5 °. No slit was present; step size of 0.022 at 1.5 steps second^{-1}, sample rotated at 15 rpm).

Thermogravimetric analysis of as-prepared samples was performed on a NETZSCH TG1000M in a dry air flow with a heating range of 5 °C min^{-1}. Elemental analysis was carried out by Elemental Analysis Service, London Metropolitan University, United Kingdom. Elemental compositions of the samples were carried out on a PANalytical Axios WDXRF (wavelength dispersive X-ray fluorescence) spectrometer with a 4 kW Rh tube. Scanning electron microscopy on samples was carried out with a JEOL JSM 6700F SEM.

Detemplation of selected samples was performed in a tube furnace at a temperature ranging between 500 - 600 °C (reached via a heating ramp of 20 °C min^{-1}) for 12 h in a stream of dry oxygen. To establish the porosity of the calcined solids, adsorption isotherms for N_2 at -196.15 °C were measured using a Micromeritics Tristar II 3020 apparatus. The samples were heated under vacuum at 150 - 180 °C in order to remove physisorbed water.

Solid-state NMR spectra were recorded at 9.4 T (400 MHz) using a Bruker Avance III console, and wide-bore Bruker BB/1H WVT MAS probes; 4 mm for ^{1}H, ^{13}C, ^{27}Al, ^{31}P and 7 mm for ^{29}Si. The sample was packed into zirconia MAS rotors, which were spun using room temperature purified compressed air, at either 4 kHz (^{29}Si), 10 kHz (^{13}C, ^{31}P) or 14 kHz (^{27}Al). The sample was either used as-made (^{13}C), dried overnight at 110 °C (^{27}Al, ^{29}Si, ^{31}P, calcined sample), or dried overnight at 150 °C (^{27}Al, as-made sample). ^{27}Al, ^{29}Si and ^{31}P spectra were acquired using a single pulse (90° pulse for ^{29}Si and ^{31}P, 22.5° pulse for ^{27}Al) without ^{1}H decoupling. The ^{13}C spectrum was recorded using ramped cross-polarisation (CP) from ^{1}H in a contact time of 1 ms, with ^{1}H decoupling using the SPINAL-64 sequence during acquisition of the ^{13}C signal. Recycle delays were 3 s (^{13}C), 0.5 s (^{27}Al), 240 s (^{29}Si) and 200 s (^{31}P). ^{13}C and ^{29}Si spectra were referenced to neat tetramethylsilane, using secondary references of the L-alanine carboxylate resonance at 177.8 ppm, and kaolinite at -91.2 ppm, respectively. ^{27}Al spectra were referenced to 1 M Al(NO$_3$)$_3$ (aq) using a secondary reference

of yttrium aluminium garnet at 0 ppm. [31]P spectra were referenced to 85% H_3PO_4 using a secondary reference of $NH_4H_2PO_4$ at 0.9 ppm.

Crystallography: Rietveld refinement

For structural analysis and refinement purposes, samples were loaded in 0.7 mm diameter quartz glass capillaries and dehydrated at $170 - 250$ °C under a vacuum of 10^{-5} mbar for 10 h before being sealed. For the calcined STA-20, a sample was detemplated at 550 ºC in dry oxygen. Upon cooling, the O_2 was switched to N_2 and when at temperatures below 50 ºC the N_2 was bubbled through hexane before being passed over the calcined solid, resulting in adsorption of hexane by the solid. This prevents hydration of the sample prior to loading into the capillary. The adsorbed hexane was then removed upon gradual heating under vacuum on the glass line, as described above. X-ray powder patterns were measured in Debye-Scherrer mode at station I11 at the Diamond synchrotron using monochromated X-rays ($\lambda = 0.8258$ Å) and a MythenII position sensitive detector.[31,32]

Rietveld refinement of dehydrated as-prepared and calcined samples was carried out using the GSAS suite of programs.[33,34] The background was fitted using Chebyschev or cosine functions and the peak profiles were modelled using a Pseudo-Voigt function.[35]

Transmission Electron Microscopy

Transmission electron microscope images and selected-area electron diffraction (SAED) patterns were obtained using a JEOL JEM-2011 electron microscope operating at an accelerating voltage of 200 kV. The images were recorded using a Gatan 794 CCD camera.

Spherical aberration corrected (C_s-corrected) high angle annular dark field scanning transmission electron microscopy (STEM-ADF) measurements were made on an X-FEG TITAN FEI 60-300 transmission electron microscope operated at 300 kV. The column was fitted with a CEOS spherical aberration corrector for the electron probe which was aligned using a gold standard sample prior to every experiment. The microscope also incorporated a Gatan Tridiem energy filter, an EDAX EDS and a Fischione HAADF detector. The half-angle employed was 17.5 mrad. The values extracted for the different aberrations were A1 < 2 nm; A2 and B2 < 20 nm, C3 -500 nm; S3 and A3 < 600 nm allowing a measured probe size of 0.78 pÅ. The total time for each of the images presented here did not exceed 10 seconds with 1024 × 1024 pixels per micrograph. The dose employed was kept below 10 pA and the collection angle was set to 30 mrad (inner) and 200 mrad (outer).

Computational Modelling

In order to understand the co-templating action of the diDABCO-C6 and trimethylamine molecules for STA-20, molecular modelling studies were performed using the Forcite module within the program Materials Studio version 6.1.[36] The Constant Valence Force Field (CVFF) was used and the framework structure was simulated using a fully aluminophosphate model with an aluminium to phosphorus ratio of 1:1. Negative charges were spread across all the atoms in the framework so that a neutral simulation box was maintained upon introduction of diDABCOs with a +2 charge and the crystal symmetry was decreased to *P*1 to allow full freedom of motion of the organic molecules. The framework atoms were held rigid throughout the simulation. Energy minimisation was performed following a simulated annealing protocol that ran for 100,000 steps at temperatures of 476.85 °C, 226 °C, 26.85 °C and −173.15 °C. The time step used was 1×10^{-15} s.

For comparison, the lattice energies of the frameworks of STA-20 and similar 12-layer ABC-6 topology types were calculated, in the SiO_2 composition, using the GULP[37] program using the 3-body interatomic potentials derived by Sanders et al,[38] as implemented within the Materials Studio software.[36]

Results

Synthesis

The first appearance of STA-20 was as an impurity phase during the synthesis of SAPO STA-18 (SFW) using trimethylamine (TrMA) and diDABCO-C6, using a gel composition of $Al(OH)_3$: 0.8 H_3PO_4 : 0.2 SiO_2 : 0.1 (diDABCO-C6)Br_2 : 0.13 TrMA : 0.28 TBAOH : 40 H_2O (using Aldrich, fumed silica and Aldrich (40 wt.% in H_2O) as sources of aluminium hydroxide, silica and TBA, respectively) and crystallized under static conditions for 190 °C for 48 h. Subsequently, it was found that STA-20 could be prepared under static conditions with least impurities by reducing the temperature to 160 ºC and using a Si/Al ratio of 0.2, a TrMA/Al ratio of 0.4–0.5 and sufficient TBAOH to bring the initial pH to 7.

Further improvement of the reproducibility of the synthesis of STA-20 was achieved by rotating the autoclaves during heating, reducing the SiO_2 content, and using different sources of $AlOH_3$, SiO_2 and TBAOH. The optimized gel composition was $Al(OH)_3$: 0.9 H_3PO_4 : 0.1 SiO_2 : 0.1 (diDABCO-C6)Br_2 : 0.42 TrMA : 0.08 TBAOH : 40 H_2O with 2.0 wt. % of SAPO-56 seeds (using Alfa, fumed silica and Sachem (55 wt.% in H_2O) as sources of aluminium hydroxide, silica and TBA, respectively), and the optimized procedure is as described in the Experimental Section. Under these conditions, SAPO STA-20 was obtained as a microcrystalline powder, with hexagonal prismatic crystals a few microns across and less than a micron thick (Figure S1). The laboratory PXRD of as-prepared STA-20 is shown in

Figure 1. Details of all syntheses and product phases during this optimization procedure are given in Table S1.

The SAPO-56(AFX) seeds added in these preparations accelerate the crystallization of STA-20 compared to that of competing phases such as SAPO-31 and AlPO-21 and thereby improve the phase purity of the product: STA-20 can form without seeds, but often with impurity phases. Similar effects were previously observed for co-templated syntheses of SAPOs STA-18 (SFW) and STA-19 (GME).[30] Other materials with frameworks belonging to the ABC-6 family, such as SAPO STA-18 and STA-20, can also be successfully used as seeds for STA-20. We speculate that the similar structural layers present in these materials play a role in the nucleation of STA-20 crystals.

To investigate the role of TrMA under these conditions, a synthesis was performed in the absence of TrMA, increasing the TBAOH content in order to maintain a neutral pH. The composition of the starting gel was 1.0 Al(OH)$_3$: 0.9 H$_3$PO$_4$: 0.1 SiO$_2$: 0.1 (diDABCO-C6)Br$_2$: 0.28 TBAOH : 40 H$_2$O. PXRD shows SAPO-31 (ATO-type) was the main phase to crystallise (Figure S2(a)), indicating the crucial structure-directing role played by TrMA in the crystallization of SAPO STA-20. Notably, during the preparation of SAPO-56 (AFX-type) and SAPO STA-18 (SFW) in the absence of trimethylamine, the main phase to crystallise was AlPO-5 (AFI). [30]

To determine whether STA-20 could crystallize with an AlPO$_4$ framework composition, a gel with composition 1.0 Al(OH)$_3$: 1.0 H$_3$PO$_4$: 0.1 (diDABCO-C6)Br$_2$: 0.42 TrMA : 0.08 TBAOH : 40 H$_2$O was heated at 160 ºC for 48 h. AlPO-21 (AWO) was the principal phase to form together with STA-20 as a minor impurity (Fig. S2b). AlPO-21 is a small pore material, with 1-dimensional 8R channels (opening 4.0 x 2.7 Å) running parallel to the *a*-axis. AWO does not belong to the ABC-6 family of framework structures and it does not contain *gme*

cages in its structure. However, the size and shape of the *awo* cage are similar to those of *gis*, and consequently it can accommodate trimethylamine. The lack of negative charge within the framework due to the absence of Si atoms might disfavour the double positively charged diDABCO-C6 from templating the *sta-20* cage.
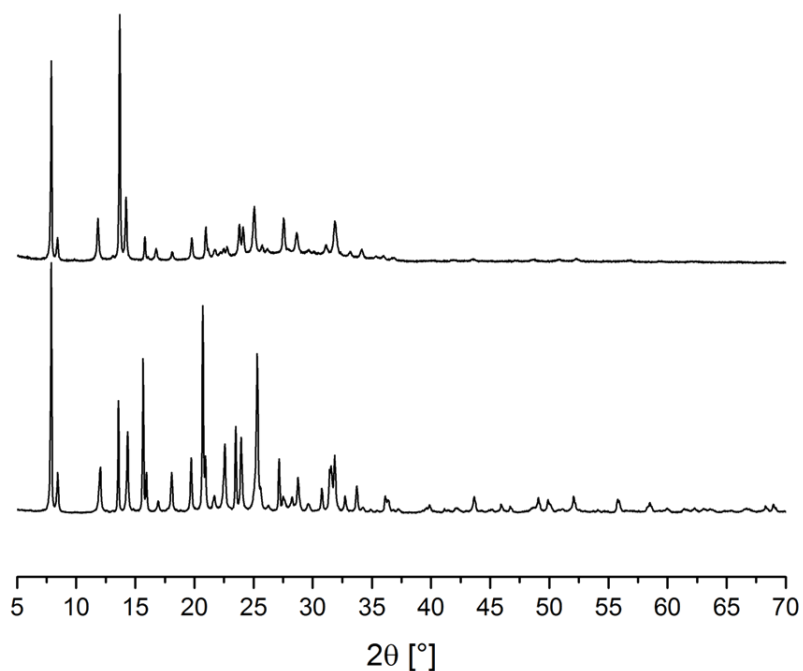

Figure 1. PXRD patterns of as-made (bottom) and calcined (top) SAPO STA-20.

Upon calcination to remove the template, STA-20 retains crystallinity (Fig. 1). The nitrogen adsorption isotherm measured volumetrically on calcined SAPO STA-20 (protected against water adsorption after calcination by adsorption of hexane and subsequently heated under vacuum to remove the alkane) is shown in Figure S3. The N_2 uptake at $p/p_0 = 0.2$ corresponds to 4.9 mmol g^{-1}, indicating an internal pore volume of 0.17 cm^3 g^{-1}. The calculated BET surface area was 333 m^2 g^{-1}. These values obtained are comparable with those measured for calcined SAPO-56 and SAPO STA-18.[30]

Determination of the Framework Structure of STA-20

The crystallites of STA-20 were too small for single-crystal X-ray diffraction, so selected area electron diffraction was performed on crystals of as-prepared STA-20 to determine the unit cell. Electron diffraction patterns were obtained with the electron beam incident perpendicular to the platy crystals laid flat on the microscope grid (down the [001] zone axis) and also onto crystallites oriented 'edge-on' to the beam (a direction subsequently established as down the [100] axis) (Fig. 2). From this diffraction a trigonal/hexagonal unit cell with a = 12.92 - 12.95 Å and c = 30.31 - 30.50 Å was derived. Moreover, the SAED pattern collected along the [100] zone axis shows a more intense spot every four spots along [001], corresponding to a strong repeat corresponding to ¼ of the c-axis, or 7.5 Å. This suggested the structure was made up of *gme* cages, particularly in the light of our previous observation that trimethylamine is a strong template for this cage. The electron diffraction patterns do not show streaking, indicating the stacking sequence is well ordered.
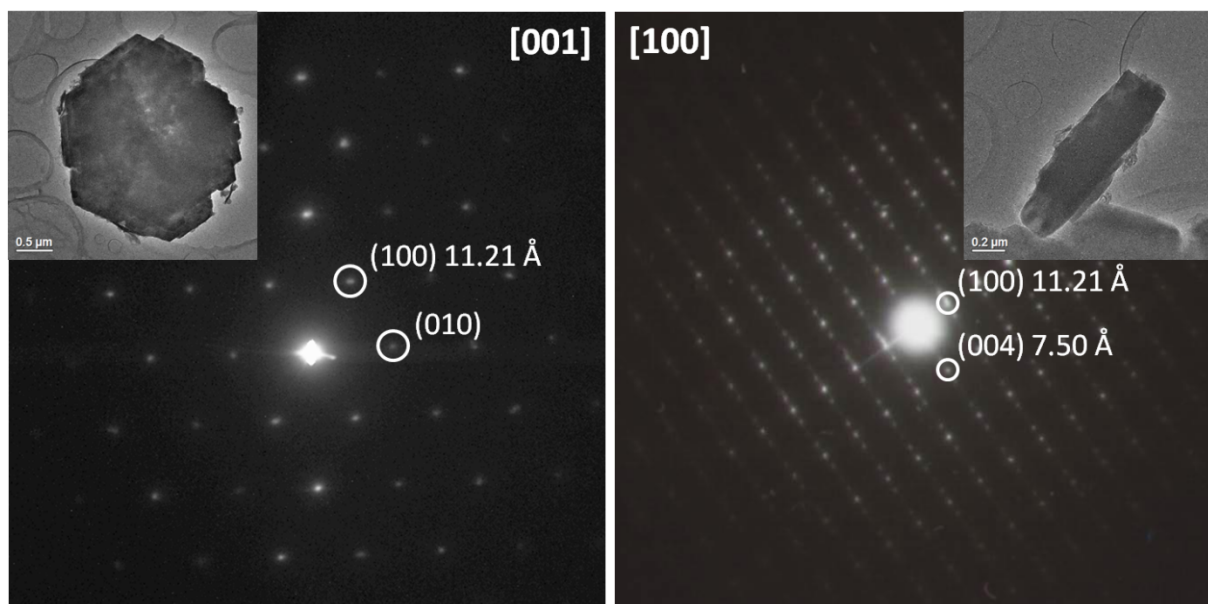
Figure 2. Selected-area electron diffraction (SAED) of SAPO STA-20 crystals collected along (left) [001] and (right) [100] directions. Inserts show TEM images of the corresponding crystals for the SAED patterns.

X-ray powder diffraction data collected on a sample of as-made STA-20 were analysed using the FullProf suite of programs.[39] Twenty-five peaks were chosen in the 2θ range 5 - 40° and a cell with lattice parameters $a = b = 13.219$ Å, $c = 30.0501$ Å, $\alpha = \beta = 90°$, $\gamma = 120°$, was found using the algorithm DICVOL 06 in Fullprof[39] (Fig. S4). These unit cell parameters suggested SAPO STA-20 is a member of the ABC-6 family. All nineteen ABC-6 structures reported in the Zeolite Structure Database[12] can be indexed using a hexagonal (or trigonal) lattice with a in the range of 13 ± 1 Å. The length of the c-axis is closely related to the ABC stacking sequence. The average layer thickness corresponds to ~2.5 Å. Moreover, the lengths of their a-axes vary as a function of the number of 6R and D6R layers in the stacking sequence: 6Rs only, $a =12.25$ - 12.70 Å; 6Rs and D6Rs, $a = 12.85$ - 13.20 Å and D6Rs only, $a = 13.65$ - 13.75 Å. Based on these assumptions, a- and c-axes of STA-20 suggested that the framework belongs to the ABC-6 series and consists of 12 layers (30.05 Å/2.5 Å ~ 12) which include 6R and D6R layers.

To determine the framework structure, the lattice parameters within the range $a = b = 12.8$ - 13.3 Å and $c = 29.0$ - 31.0 Å were loaded within the Atlas of Prospective Zeolite Structures Database.[40] After a careful analysis of the 99 results, it was found that the hypothetical 'SiO$_2$' ABC-6 structure having code 194_3_1140 showed all the desired features: a 12-layer stacking sequence AABAABAACAAC with 7.5 Å sub-unit repeats, consistent with the strong intensity in the electron diffraction corresponding to a 7.5 Å repeat unit, *gme* cages expected to host trimethylamine co-templates and a cage the length of three 8Rs long enough to host extended OSDAs. The topology also contains *d6R* and *can* cages.

To investigate how unique this structural model is, additional topologies consistent with the synthetic details and the experimental diffraction data were examined. Li *et al*. enumerate

eighty-five 12-layered topology types, giving their predicted unit cells. From this, many possibilities with short *a*-axis repeats or those lacking *gme* cages can be eliminated. Furthermore, our previous modelling work indicates that the OSDA used in this work, diDABCO-C6, favours long cages but does not fit well into cages with less than a 9-layer repeat, and these facts enable the possible topology types to be further narrowed down to just a few candidates, with that identified from the hypothetical database the most likely.

Further confirmation of the proposed model was obtained by high resolution transmission electron microscopy, which until recently was not thought to be suitable for imaging beam sensitive materials such as aluminophosphates at atomic resolution. Images with atomic resolution were obtained by the C_s-corrected STEM-ADF method described elsewhere,[41-43] and applied here for the structural elucidation of an unknown zeotype. Figures 3a, b and c correspond to a STA-20 crystal orientated along the [100] zone axis allowing a clear visualization of the atomic columns while Figures 3d, e and f show the orientation along the [001] zone axis. For clarity Figure 3b has been Wiener filtered in order to improve the signal to noise ratio; Figure 3c and f are an enlarged micrograph of 3b and e, respectively. These images can be matched to the proposed framework structure and those taken along the [100] axis enable the stacking sequence AABAABAACAAC to be read off directly, because the STEM-ADF image reveals the projected positions of the tetrahedral cations. It does not show the lower atomic number oxygen anions. Furthermore, images taken over an extended area show that the material is very well ordered, so that the suggested structure is a good starting point for subsequent structure refinement. Similar observation was performed in another crystal tilted along the [001] zone axis, which were Fourier filtered for clarity. Superposition of the STA-20 framework on the STEM images down [100] and [001] zone axes, together with the associated electron diffraction patterns, are given in Figure S5.
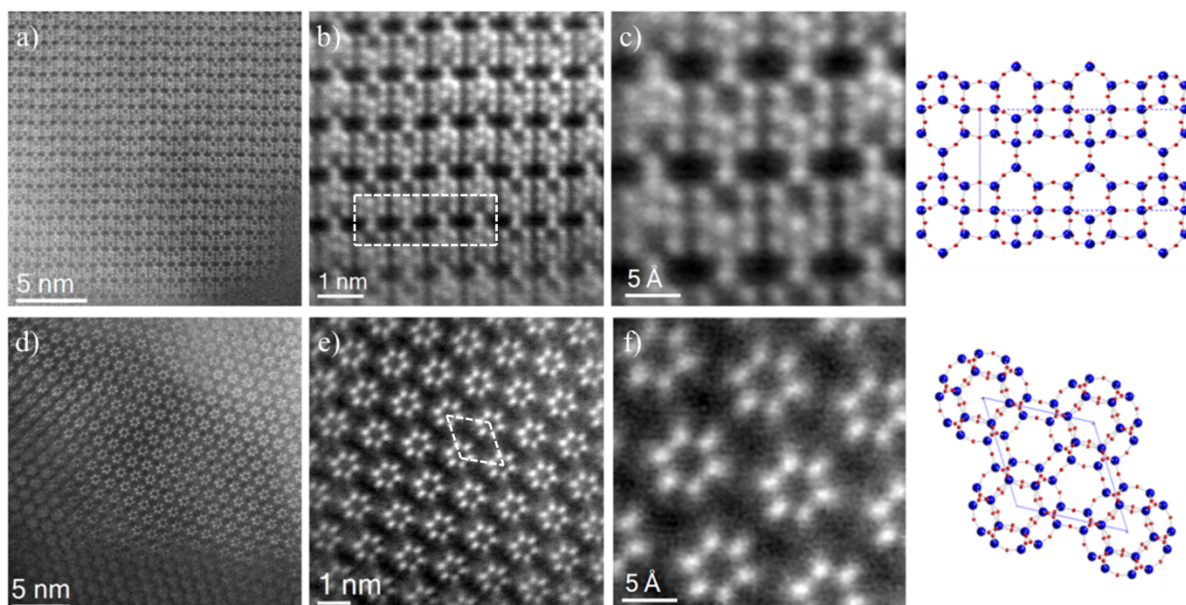
Figure 3. C$_s$-corrected STEM-ADF images of SAPO STA-20 taken along the [100] (a, b and c) and [001] (d, e and f) zone axes. The same projections of the STA-20 frameworks are shown on the right for comparison (Si blue, O red). The images were Wiener or Fourier filtered to reduce noise.

Structure Refinement of Calcined STA-20

Initially, the dehydrated, calcined material was examined by Rietveld refinement, because removal of the organic content results in a more straightforward structural refinement. Chemical analysis indicates a unit cell composition (assuming the framework model to be correct, and without including H) of $Al_{37}P_{33}Si_2O_{144}$, within experimental error of Al : (P+Si) of 1 : 1. Solid-state ^{27}Al and ^{31}P MAS NMR (Fig. S6) indicate both Al and P are tetrahedrally-coordinated: The relevant narrow signals are ^{27}Al (Al(OP)$_4$) at 33 ppm and ^{31}P (P(OAl)$_4$) at -34.6 ppm. The ^{31}P shows a broad resonance from around -20 ppm to -30 ppm which may come from a less crystalline component. The range of peak positions observed is consistent with published values for AlPO$_4$ materials. The broad resonance between −60 and −130 ppm

observed in the ^{29}Si MAS NMR spectrum (Fig. S6) is consistent with the presence of silica islands and/or amorphous silica.

The symmetry of 194_3_1140, modelled as pure SiO_2, is *P6$_3$/mmc*. This has to be changed to *P*-31*c* to accommodate the strict alternation of Al and P (or Si) atoms within the framework. This model was then used as a starting point for the successful Rietveld refinement of the structure against synchrotron PXRD data using GSAS.[33,34] Geometric restraints were imposed on atom-atom distances of framework atoms as detailed in the Experimental section. The final fit is shown in Figure 4 and crystallographic details are listed in Table 1.
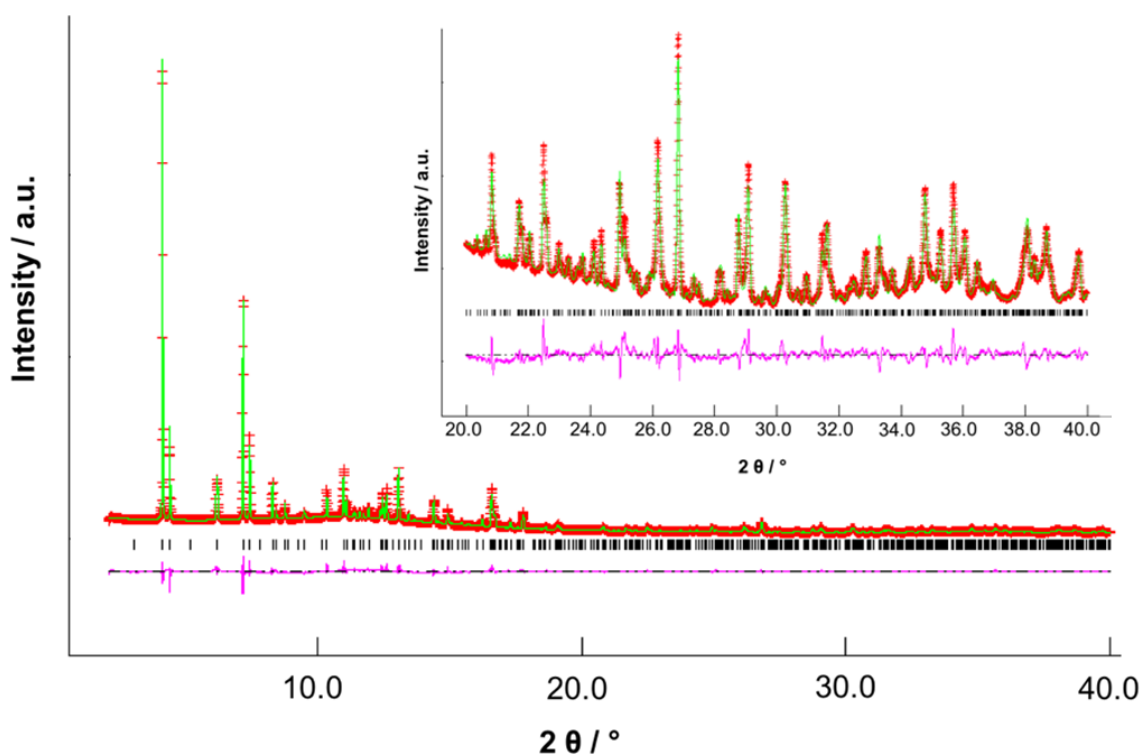
Figure 4. Rietveld refinement of calcined, dehydrated STA-20 against synchrotron PXRD data (λ = 0.826163 Å). Space group *P*- *31c*, *a* = 13.15497(18) Å, *c* = 30.5833(4) Å, R_{wp} = 4.69 %. Red crosses = experimental data, green line = simulated data, black tick marks = predicted peak positions, magenta line = difference profile.

Table 1. Crystallographic data for as-prepared and calcined dehydrated SAPO STA-20 synthesised using trimethylamine and diDABCO-C6 as SDAs.

|	SAPO STA-20 as-prepared, dehydrated	SAPO STA-20 calcined, dehydrated
Chemical composition	$[diDABCO\text{-}C6]_{1.9}[TrMA]_{3.8}$ $Al_{36}P_{30.4}Si_{5.6}O_{144}$	$Al_{36}P_{30.4}Si_{5.6}O_{144}$
Data collection		
Wavelength / Å	0.826163	0.826163
Diffractometer geometry	Debye-Scherrer	Debye-Scherrer
Sample	Rotating 0.7 mm capillary	Rotating 0.7 mm capillary
Refined region / $2\theta°$	2.0–92.0	2.0–92.0
Step size / $2\theta°$	0.01	0.01
Unit cell		
Chemical formula	$[N_1C_3H_9]_2[N_{3.7}C_{16.8}H_{33.7}]_2$ $Al_{36}Si_{7.2}P_{28.8}O_{147.1}$	$Al_{36}Si_{7.2}P_{28.8}O_{144}$
Crystal system	trigonal	trigonal
Space group	$P\text{-}3\,1\,c$	$P\text{-}3\,1\,c$
a / Å	13.17399(11)	13.15497(18)
b / Å	13.17399(11)	13.15497(18)
c / Å	30.0927(9)	30.5833(4)
Volume / Å^3	4523.00(16)	4583.48(13)
Rietveld refinement		
Refined region / $2\theta°$	2.0–60.0	2.0–40.0
Excluded regions / $2\theta°$	13.05–13.39, 24.90–25.64, 26.78–27.16	
Background	Chebyschev 36 terms	Cosine Fourier 36 terms
R_{wp}	0.0568	0.0469
R_p	0.0378	0.0356
R_F^2	0.1261	0.1207

Framework Structure of SAPO STA-20

The 6R stacking sequence of STA-20 results in a structure that consists of two different types of columns of cages that run parallel to the crystallographic *c*-axis, and this is represented in Figures 5 and 6. The first column type, which passes through the origin of the unit cell at the position (x = 0, y = 0) in a projection on the *ab* plane (A site), consists of alternating *can* cages and *d6r* units, with two *can* cages in a sequence having the same orientation while the next two are rotated by 60°, so that in a unit cell the sequence along *c* is *can-d6r-can-d6r-can(R60°)-d6r-can(R60°)-d6r*. The second column type, which occupies the space between chains of the first type, consists of alternating *gme* and *sta-20* cages and runs along the *c*-axis through B (1/3, 2/3) and C (2/3, 1/3) in projection on the *ab*-plane. There are two columns of

the second type for every column of the first type (Figure 5). STA-20 is the second member of the ABC-6 family to be discovered that contains four different types of cages in its structure: *d6r*, *can*, *gme* and *sta-20* cages. The other member is AlPO-52 (AFT) which contains *d6r*, *gme*, *cha* and *aft* cages. Li et al. speculated that a feasible ABC-6 structure should contain no more than four types of ABC-6 cages:[16] STA-20 does not violate this suggestion.
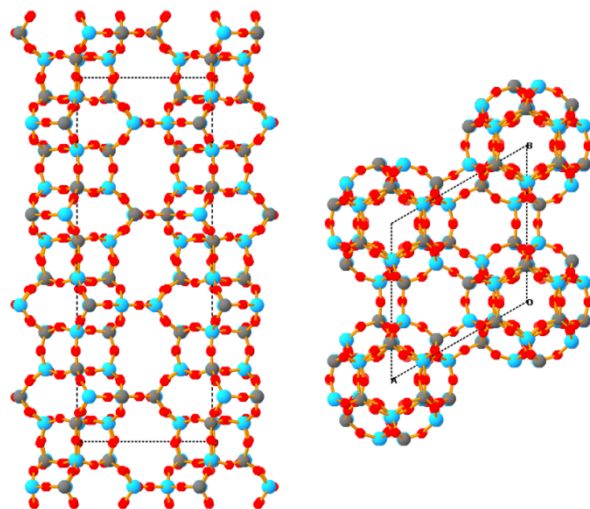
Figure 5. Refined structure of calcined SAPO STA-20, viewed perpendicular to (left) and parallel to (right) the *c*-axis with ball-and-stick representations. (light blue, Al; dark grey, P; red, O).
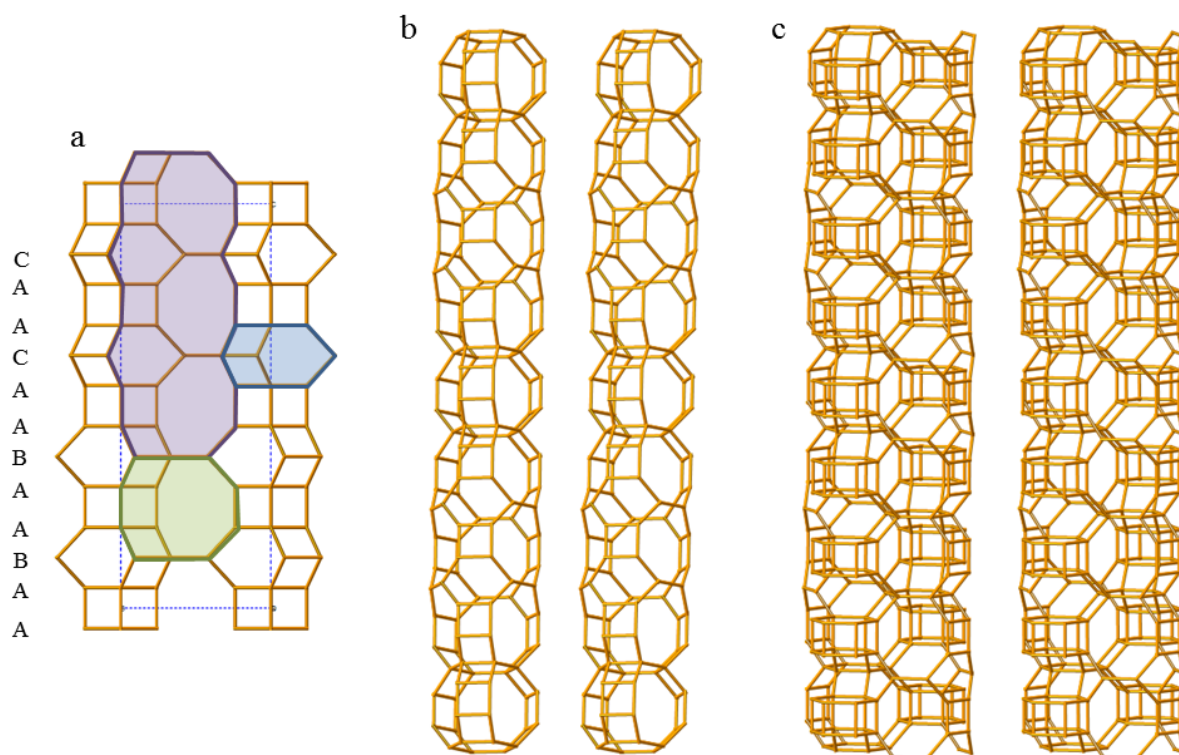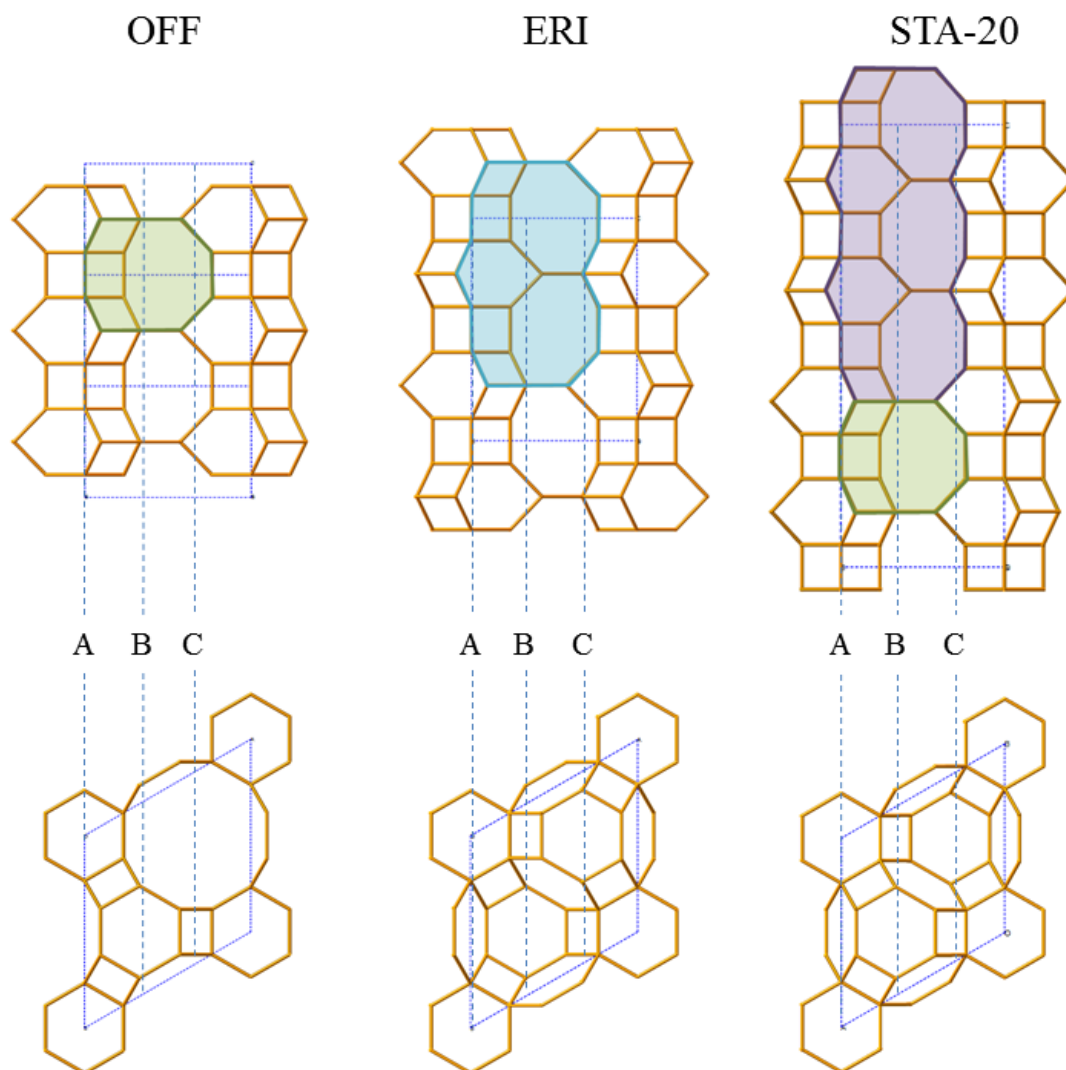
Figure 6. (a) STA-20 framework structure viewed down *a*-axis, showing the three different types of cages (green: *gme*; blue: *can*; violet: *sta-20* cage). The stacking sequences of the 6R layers are given on the left. Stereoplots (b) and (c) show the column of secondary building units and cages joined parallel to the *c*-axis and the way in which adjacent columns are linked, respectively. Oxygen atoms omitted for clarity.

The approximate cavity size (length × cross sectional diameter, minus the van der Waals radii of 1.35 Å per O atom) is 20.18 × 6.67 Å for the *sta-20* cage and 6.71 × 5.01 Å for the *gme* cage. The *sta-20* cage is 1.7 Å longer than the *sfw* cage (SSZ-52 and STA-18) that was recently assigned as the longest cavity observed in the ABC-6 family, so that STA-20 possesses the longest cage of the ABC-6 family. The largest openings in the structure are the nine 8R openings in each *sta-20* cage; six lead to other *sta-20* cages (*ca.* 5.10 Å × 3.37 Å) and

three to *gme* cages (ca. 5.01 Å × 3.27 Å). STA-20 therefore has a three-dimensionally connected small pore (8R) channel system as shown by the stereoplot in Figure 6.

The twelve layer 6R stacking sequence of STA-20 (AABAABAACAAC) is the equal longest stacking sequence in the subfamily of ABC-6 structures consisting of 6Rs and D6Rs, on a par with that of STA-2 (SAT). SAPO STA-20 is characterised by a framework density (defined as the number of T-atoms per 1000 Å^3) of 15.7, which is higher than those of other ABC-6 materials whose repeated stacking sequences can be described using only D6Rs (such as AlPO-52 (14.9) and SAPO-56 (14.7)).[14,15]

The arrangement of building units and cages in STA-20 is closely related to those of offretite (OFF) and particularly erionite (ERI). The three structures are shown in Figure 7. All three structures consist of alternating *can* cages and *d6r* units in the A position, but there are differences in the orientations of the *can* cages in the three structures. As a result, while OFF has a column of *gme* cages in the B site, and a 12R-channel centred at C, ERI has columns of *eri* cages in B and C sites and STA-20 has columns of alternating *gme* and *sta-20* cages along both B and C sites.

Figure 7. OFF, ERI and STA-20 framework structures viewed down a- and c-axes, showing the different types of cages (green: *gme*; light blue: *eri*; violet: *sta-20*) and their relative position along the hexagonal *ab*-plane: A (0, 0, 0), B (2/3, 1/3, 0) and C (1/3, 2/3, 0). Oxygen atoms omitted for clarity.

Structure Solution and Refinement for As-Prepared STA-20

The unit cell parameters of as-prepared STA-20 are very similar to those of the calcined material, so the framework structure was expected to be the same. To fit the diffraction pattern, however, a model of the structure including the organic structure directing agents is

required. This was achieved using a combination of solid state NMR, chemical analysis and computational modelling.

The solid-state ^{13}C MAS NMR spectra of as-prepared STA-20 is consistent with the incorporation of both TrMA and diDABCO-C6 templates within the STA-20 framework (Fig. 8, with full assignment), and can be related to that observed previously for STA-18 (SFW) prepared with the same co-templates.[30] Most signals observed in STA-20 are closely similar to those non-equivalent C atoms assigned to diDABCO-C6 in STA-20. However, for each expected non-equivalent C in diDABCO-C6 in STA-20, two peaks can be resolved in the spectrum. This indicates either the molecule is in an asymmetric environment, or that the molecule is present in two distinct configurations or states within the zeolite framework structure. The N(CH$_3$)$_3$ resonance at 46.9 ppm was assigned to TrMA, shifted to lower frequency compared to the 47.8 ppm observed in SAPO-56, STA-18 and STA-19 prepared using the co-templating approach.[30]

In the ^{27}Al MAS NMR spectrum of the as-prepared sample (Fig. S7), two main signals are present: one at 37.5 ppm assigned to tetrahedrally-coordinated Al atoms and one at 15.6 ppm assigned to five-fold Al. The additional coordination is likely to be from charge-balancing hydroxyl groups, because it is not removed by dehydration at 150 °C.
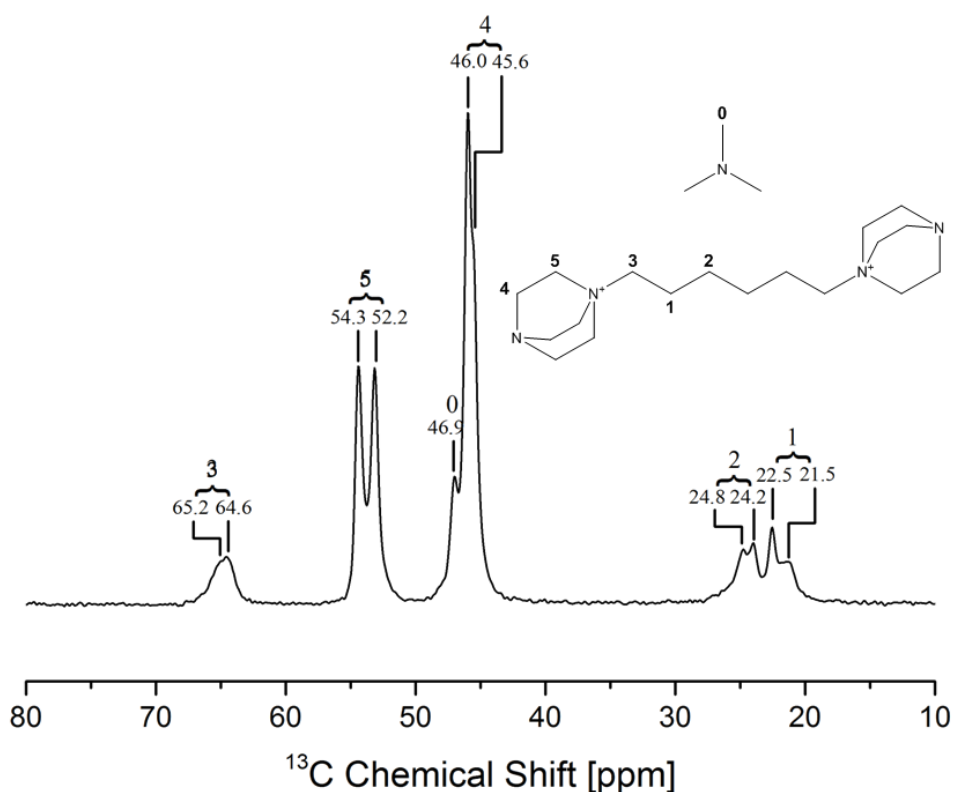
**Figure 8.** Solid-state ^{13}C MAS NMR spectrum for dehydrated as-prepared SAPO STA-20, with suggested assignments.

Elemental (CHN) analysis, including a measured C/N ratio of 3.45, combined with TGA and XRF indicates a unit cell composition of [diDABCO-C6]$_{1.96}$[TrMA]$_{3.66}$Al$_{37.4}$P$_{32.9}$Si$_{1.7}$O$_{144}$ 4H$_2$O. Remarkably, this suggests that TrMA does not only occupy *gme* cages (of which there are two in the unit cell) but must also occupy sites in the larger cages. (A simple model with 100% occupancy of TrMA in *gme* and diDABCO-C6 in *sta-20* cages would give a C/N ratio of 3.6). Molecular modelling studies were used to investigate this further. The minimum energy configuration of diDABCO-C6 was modelled in the *sta-20* cage and, for comparison, in the *sfw* cage of STA-18 (SFW), which had been observed experimentally. The SDA gives comparable energies for the two configurations (Fig. S8) with binding energies per mole of SDA of -173 kcal mol^{-1} in STA-20 *cf.* -155 kcal mol^{-1} in STA-18 (SFW). However, additional space is available in the longer *sta-20* cage, and the question arose whether this would be

sufficient to hold an additional TrMA molecule, as suggested by the compositional measurements. Two structural models were therefore generated computationally (Fig. S9). In the first, diDABCO-C6 and TrMA were included in the *sta-20* and *gme* cages, respectively, and their energies minimised. In the second, a TrMA molecule was included into each *sta-20* cage along with the diDABCO-C6 molecule, as well as in the *gme* cages. These were used as starting models for Rietveld refinement against synchrotron PXRD data of dehydrated as-prepared STA-20.

During the refinements, the positions of the templates were kept constant and only their occupancy was allowed to refine. A slightly better fit (Fig. 9) was achieved for the model including TrMA molecules in the *sta-20* cages as well as in the *gme* cages, shown in Figure 10. Furthermore, one extra-framework site for an oxygen atom within the *can* cage was found by difference Fourier analysis (Fig. S10). Although slightly too far away from the Al atoms and probably in a disordered average position, the oxygen atom might correspond to charge-balancing hydroxyl groups suggested by ^{27}Al MAS NMR. Similar bridging hydroxyl oxygen atoms were previously found within the *can* cage of AlPO-17[44] and AlPO STA-2[45] prepared with the SDAs N,N,N´,N´-tetramethyl-1,6-hexanediamine and diDABCO-C4, respectively. Attempts to search for further sites via Fourier analysis were not successful.

Crystallographic data are listed in Table 1. The final atomic coordinates and thermal parameters for as-prepared and calcined SAPO STA-20 are listed in Table S2 and Table S3, respectively. Their selected interatomic lengths and angles are summarised in Table S4 and Table S5, respectively.
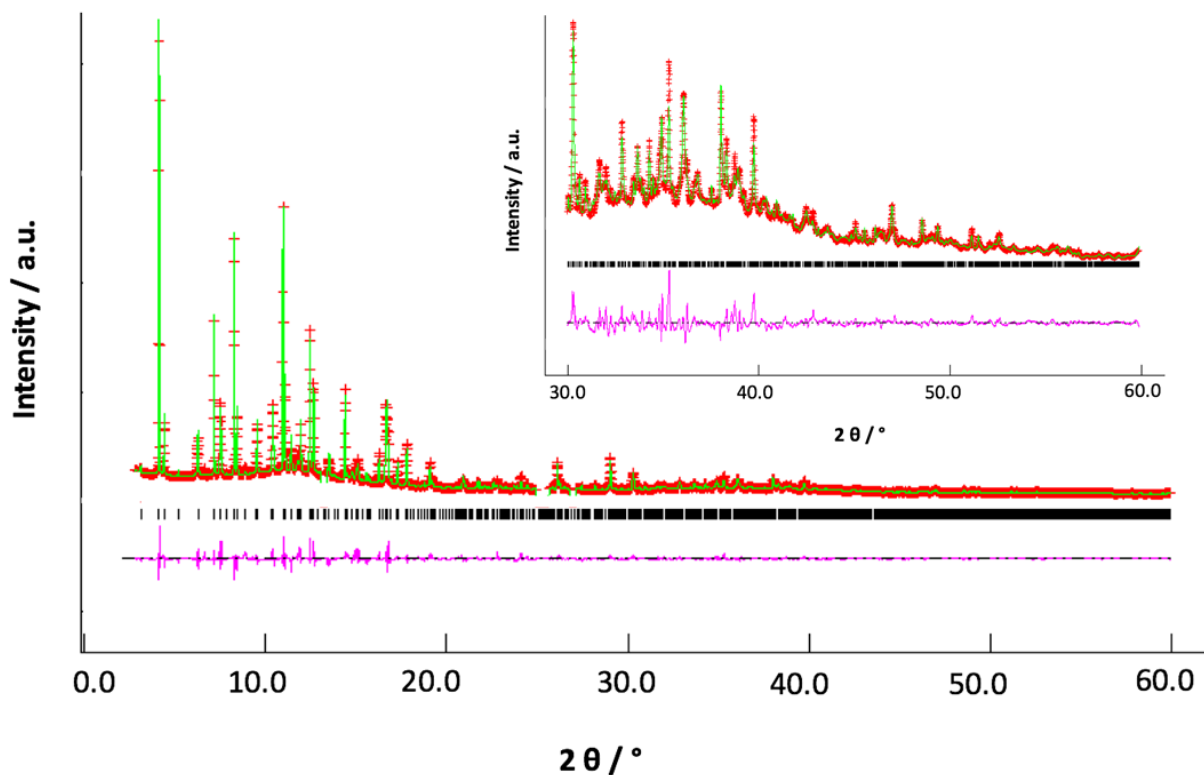
Figure 9. Rietveld refinement against synchrotron data (λ = 0.826163 Å) for as-prepared, dehydrated STA-20. Space group P-31c, a = 13.17399(11) Å, c = 30.0927(9) Å, R_{wp} = 5.70 %. Red crosses = experimental data, green line = simulated data, black tick marks = predicted peak positions, magenta line = difference profile.
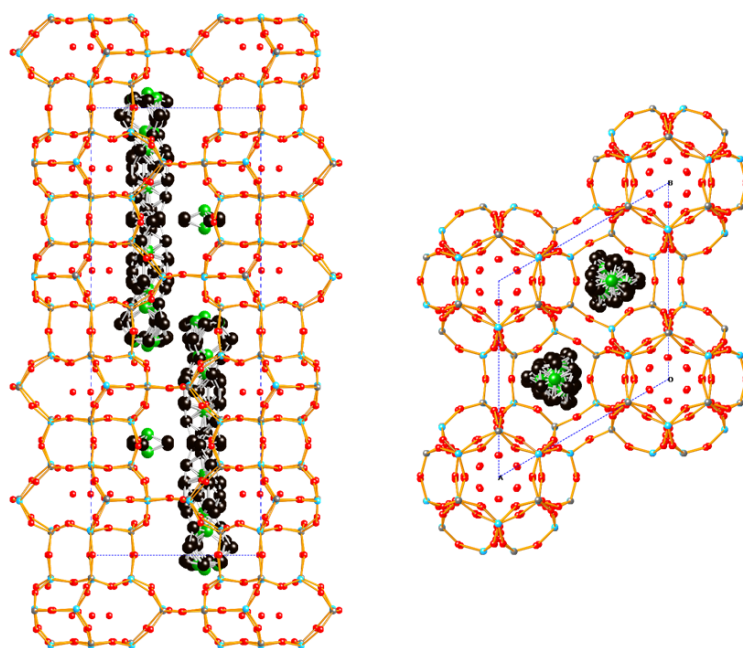
Figure 10. Structure of as-prepared SAPO STA-20, viewed down *a*- (left) and *c*-axes (right), with ball-and-stick representations of trimethylamine and diDABCO-C6 in the *gme* and *sta-20* cages. (Al light blue, P dark grey, O red, C black, N green; H atoms are omitted for clarity; template atoms shown with disorder over symmetrically equivalent positions).

A consideration of the 12-layer polytypes in the ABC-6 system shows that two other stacking sequences, denoted MS-1 and MS-2 (recently listed in the Li et al. database,[16] codes 183 and 184 respectively), contain similar *d6r*, *can*, *gme* and *sta-20** cages to those in STA-20. The *sta-20** cages in MS-1 and MS-2 have the same length as *sta-20* but the sequence of D6R (d) and 6R (s) along the cage walls are different: STA-20 dsdsd, MS-1 ddssd and MS-2 dssdd. The three structures with their relative stacking sequences and distribution of building units on the *ab*-plane are shown in Figure 11 and Table 2. To have a better understanding of the reason for the crystallisation of the specific stacking sequence AABAABAACAAC(A) by STA-20, and not one of the other two possibilities, the three framework structures, considered as pure silicates in *P*1 symmetry, have been energy minimised at isochoric and isobaric conditions by GULP calculation. The energy value at constant volume for the 194_3_1140

model is −9256.55 eV whereas the MS-1 and MS-2 models give energies of −9254.96 and −9255.11 eV, respectively. This shows that the structure determined for STA-20 is 1.59 eV (153.4 kJ mol^{-1}) and 1.44 eV (138.9 kJ mol^{-1}) more stable than those of MS-1 and MS-2, respectively. The same trend was also observed for the energy minimisation conducted at constant pressure: 1.55 eV (149.6 kJ mol^{-1}) with MS-1 and 1.38 eV (133.2 kJ mol^{-1}) with MS-2. These energy calculations are therefore consistent with the identification of the structure of STA-20 achieved by atomic-resolution electron microscopy (Fig. 3).

Table 2. Three possible 12-layer stacking sequences containing *d6r*, *can*, *gme* and *sta-20/sta-20** cages.

model	n° of T site	space group	stacking sequence	A site	B site	C site
194_3_1140	3	*P6₃/mmc*	AABAABAACA AC(A)	*can, …*	*can, gme, …*	*gme, can, can, …*
MS-1	6	*P6₃mc*	AABBABAACC AC(A)	*sta-20*, gme, …*	*sta-20*, can, …*	*sta-20*, can, …*
MS-2	6	*P-3m1*	AABBABAACA CC(A)	*gme, sta-20*, …*	*can, sta-20*, …*	*can, sta-20*, …*
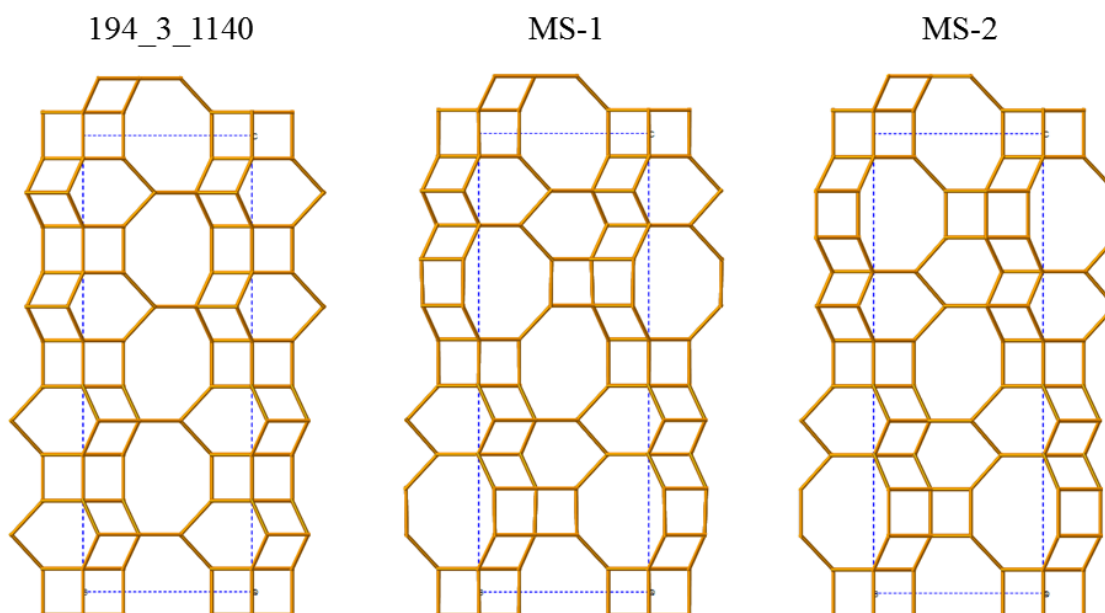
Figure 11. Three candidate structures with 12-layer stacking sequences which include 6Rs and D6Rs.

Discussion

The characterisation and crystallography reveal that a novel ABC-6 polytype with a three dimensionally-connected pore system and silicoaluminophosphate composition has been prepared using a combination of trimethylamine and diDABCO-C6 in the hydrothermal synthesis. Solid-state ^{13}C NMR and chemical analysis indicates both are included in the final product. Trimethylamine is known to direct the formation of *gme* cages[30] - without it the channel structure SAPO-31 forms - while the diDABCO-C6 can only occupy the longer '*sta-20*' cages. Furthermore, elemental analysis suggests that during the crystallisation, trimethylamine is included not only in the *gme* cages but also in the '*sta-20*' cages, which are longer than the diDABCO-C6 molecules. Modelling shows that this is reasonable, and inclusion of the TrMA in the *sta-20* cages also improves the Rietveld refinement. It also provides one possible explanation for observed splitting in ^{13}C resonances from the diDABCO-C6 SDA. Incorporation of more than one organic molecule in a single cage during crystallisation has been previously proposed for the aluminosilicate SSZ-52 (SFW).[25]

Previously, co-templating (using tetramethylammonium and tetraethylammonium as co-templates) has been used to prepare the zeolite UZM-5,[46,47] with a topology type (UFI) that had at that time not been observed. The co-templating approach has been shown to give SAPOs with known topology types previously observed as aluminosilicates (GME, SFW); here we show it is possible to use this approach to access SAPOs with structure types not yet prepared in any composition. The ABC-6 structural family of SAPOs is particularly amenable to co-templating studies because cages of different sizes and shapes arise as a consequence of the different polytypic arrangements.

The details of the preparation of STA-20 are also of interest. STA-18 (SAPO (SFW)) and STA-20 may be prepared from similar gel compositions and using the same organic SDAs. This is not surprising, because both contain *gme* cages and elongated cavities, and modelling shows the diDABCO-C6 templates give similar non-bonding interaction energies in the *sfw* and *sta-20* cages. One difference between the synthesis conditions that give rise to the two structures is that STA-20 is formed from gels with lower SiO_2 contents, and so has lower Si concentrations, while the main structural difference is that STA-20 contains *can* cages, whereas SAPO (SFW) does not. The charge balance required by SAPOs with low framework silica content may be achieved by the presence of framework bound hydroxyl groups. Hydroxyl groups have previously been shown to occur in the *can* cages in the $AlPO_4$ form of the related ABC-6 structure, STA-2, and there is evidence for such species in the structural analysis of as-prepared STA-20 in this work. A second difference in the syntheses conditions is that STA-20 crystallisation is favoured over STA-18 by the use of higher TrMA : diDABCO-C6 ratios (0.4:1 to 0.5:1 *cf.* 0.13:1), even though the *gme*: longer cage ratio in STA-20 is 1 : 1, compared to 2 : 1 in the SFW structure. The co-inclusion of TrMA in the larger cages in STA-20 would make the total TrMA: diDABCO-C6 ratio the same in the two structures, assuming full occupancy.

The structure solution of STA-20 has been achieved via a multi-technique approach of the general type previously used for zeolites and zeotypes. The most remarkable additional elements in this example are the use of a hypothetical zeolite structure database and of the aberration-corrected STEM-ADF imaging technique. The use of hypothetical structure databases for structure confirmation when different framework possibilities fit the unit cell data has previously been reported.[48] In this example we used the database directly. Currently this approach is limited to structures with 6 or less crystallographically-distinct T sites for 'SiO_2' zeolites (or double this number for AlPOs where Al/P ordering results in symmetry

lowering). Whereas this was not an issue for STA-20, which has only 3 distinct Al and 3 distinct P sites, extension of the database will be required for structure solution of more complex zeolitic materials. The high quality results of the aberration-corrected STEM-ADF imaging, which directly identify the AABAABAACAAC unit cell stacking sequence of 6-ring layers, shows that it is now possible to directly image complex beam-sensitive SAPO structures. In the case of STA-20, this confirmed the structure proposed from the hypothetical database. The use of STEM-ADF, exemplified here, will open up many beam-sensitive materials to study at the atomic level, particularly when used in combination with other recent advances in electron microscopy.[49,50]

Finally, the high degree of order (and absence of stacking faults) in STA-20, illustrated by the absence of streaking in the electron diffraction patterns, indicates that organic templating can control precisely the stacking arrangement in zeolitic materials with large *c*-axis repeats, as shown previously for the SAPOs STA-2 (SAT) and STA-18 (SFW). We speculate that this is because the long templates 'overlap' in projection perpendicular to the *c*-axis, so that during growth along this direction, one set of cages begins to assemble as another is completed. Establishing the mechanism of this co-templated crystallisation requires more detailed study.

Conclusions

The synthesis of a small pore zeotype of the ABC-6 family has been achieved via the dual templating approach. Trimethylamine acts as a template for the *gme* cages in the structure, while the diDABCO-C6 acts as a structure directing agent for the *sta-20* cage, the longest observed in zeolitic ABC-6 structures. Chemical analysis suggests trimethylamine is also included along with the diDABCO-C6 molecules in these long cages: modelling gives a plausible structural model for the as-prepared material consistent with the experimental data.

The framework structure of STA-20 was elucidated via determination of the unit cell parameters (electron diffraction; powder diffraction) and subsequent identification of a candidate structural model using a hypothetical zeolite database. This model was confirmed directly by the powerful high resolution transmission electron microscopic STEM-ADF method and refined against synchrotron X-ray powder diffraction. Both hypothetical crystallography and STEM-ADF add considerably to the longer-established tools available for the structure solution of zeolites and zeotypes that crystallise as microcrystalline powders.

STA-20 possesses a 3D-connected small-pore system of the general type shown (when prepared in the appropriate chemical composition) to promote good catalytic activity for reactions such as the methanol-to-olefins conversion and the selective catalytic conversion of NO by ammonia. The ABC-6 structural family therefore continues to be a fruitful area to explore for potentially useful zeotypes and zeolites.

ASSOCIATED CONTENT

Supporting Information

The Supporting Information is available free of charge on the ACS Publications website at DOI:

Details of sample preparation, crystallography, adsorption isotherms, NMR spectra and additional figures/tables are given. The research data (and materials) supporting this publication can be accessed at DOI: http://dx.doi.org/10.17630/313df503-6c9b-486f-a2a0-e0c9f6506b50.

References

1. Moliner, M.; Martinez, C.; Corma, A. Synthesis Strategies for Preparing Useful Small Pore Zeolites and Zeotypes for Gas Separations and Catalysis. *Chem. Mater*. **2014**, *26*, 246–258.

2. Haw, J.; Song, W.; Marcus, D. M. The Mechanism of Methanol to Hydrocarbon Catalysis. *Acc. Chem. Res*. **2003**, *36*, 317–326.

3. Haw, J. F.; Marcus, D. M. Well-defined (Supra)Molecular Structures in Zeolite Methanol-to-Olefin Catalysis. *Top. Catal*. **2005**, *34*, 41–48.

4. Hereijgers, B.P.C.; Bleken, F.; Nilsen, M. H.; Svelle, S.; Lillerud, K.-P.; Bjørgen, M.; Weckhuysen, B. M.; Olsbye, U. Product Shape Selectivity Dominates the Methanol-to-Olefins (MTO) Reaction over H-SAPO-34 Catalysts. *J. Catal.*, **2009**, *264*, 77–87.

5. Castro, M.; Warrender, S.; Wright, P. A.; Apperley, D. C.; Belmabkhout, Y.; Pirngruber, G.; Park, M. B.; Min, H.-K.; Hong, S. B. Silicoaluminophosphate Molecular Sieves STA-7 and STA-14 and their Structure Dependent Catalytic Performance in the Conversion of Methanol to Olefins. *J. Phys. Chem. C*, **2009**, *113*, 15731–15741.

6. Tian, P.; Wei, Y.; Ye, M.; Liu, Z. Methanol to Olefins (MTO): From Fundamentals to Commercialization. *ACS Catal.*, **2015**, *5*, 1922–1938.

7. Bull, I.; Boorse, R. S.; Jaglowski, W. M.; Koermer, G. S.; Moini, A.; Patchett, J. A.; Xue, W. M.; Burk, P.; Dettling, J. C.; Caudle, M. T. Copper CHA Zeolite Catalysts. U.S. Patent 7601662 B2, **2009**.

8. Fickel, D. W.; D'Addio, E.; Lauterbach, J. A.; Lobo, R. F. The Ammonia Selective Catalytic Reduction Activity of Copper-Exchanged Small Pore Zeolites. *Appl. Catal. B: Environmental* **2011**, *102*, 441–448.

9. Deka, U.; Lezcano-Gonzalez, I.; Warrender, S. J.; Picone, A. L.; Wright, P. A.; Weckhuysen, B. M.; Beale, A. M. Changing Active Sites in Cu-CHA Catalysts: DeNOx Selectivity as a Function of the Preparation Method. *Microporous Mesoporous Mater.*, **2013**, *166*, 144–152.

10. Andersen, P. J.; Bailie, J. E.; Chen, H.-Y.; Fedeyko, J. M.; Shin Foo, R. K.; Rajaram, R. R. Transition Metal/Zeolite SCR Catalysts. US 8603432 B2, **2013**.

11. Ma, L.; Cheng, Y.; Cavataio, G.; McCabe, R. W.; Fu, L.; Li, J. Characterization of Commercial Cu-SSZ-13 and Cu-SAPO-34 Catalysts with Hydrothermal Treatment for NH_3-SCR of NOx in Diesel Exhaust. *Chem. Eng. J.* **2013**, *225*, 323−330.

12. Blakeman, P. G.; Burkholder, E. M.; Chen, H.-Y.; Collier, J. E.; Fedeyko, J. M.; Jobson, H.; Rajaram, R. R. The Role of Pore Size on the Thermal Stability of Zeolite Supported Cu SCR Catalysts. *Catalysis Today*, **2014**, *231*, 56–63.

13. Moliner, M.; Gabay, J. E.; Kliewer, C. E.; Carr, R. T.; Guzman, J.; Casty G. L.; Serna, P.; Corma, A. Reversible Transformation of Pt Nanoparticles into Single Atoms inside High-Silica Chabazite Zeolite. *J. Am. Chem. Soc.,* **2016**, *138*, 15743–15750.

14. Baerlocher, Ch.; McCusker, L. B.; Olson, D. H. Atlas of Zeolite Framework Types 6th Ed. Elsevier, **2007**.

15. McCusker, L. B.; Meier, W. M.; Rechsteiner, H. AB-5 and ABC-6 Networks. *Mat. Res. Bull.* **1987**, *22*, 1203–1207.

16. Li, Y.; Li, X.; Liu, J.; Duan, F.; Yu, J. In Silico Prediction and Screening of Modular Crystal Structures via a High-Throughput Genomic Approach. *Nature Comm.* **2015**, 6, Art. No. 8328.

17. Zones, S. I. Zeolite SSZ-13 and its Method of Preparation. US Patent 4,544,538, **1985**.

18. Lok, B. M.; Messina, C. A.; Patton, R. L.; Gajek, R.T.; Cannan, T. R.; Flanigen, E. M. Silicoaluminophosphate Molecular Sieves: Another New Class of Microporous Crystalline Inorganic Solids. *J. Am. Chem. Soc*. **1984**, *106*, 6092–6093.

19. Lok, B. M.; Cannan, T. R.; Messina, C. A. The Role of Organic Molecules in Molecular Sieve Synthesis. *Zeolites*, **1983**, *3*, 282−291.

20. Moini, A.; Schmitt, K. D.; Valyocsik, E. W.; Polomski, R. F. The Role of Diquaternary Cations as Directing Agents in Zeolite Synthesis. *Zeolites*, **1994**, *14*, 504−511.

21. Lobo, R. F.; Zones, S. I.; Davis, M. E. Structure Direction in Zeolite Synthesis. *J. Incl. Phen. Mol. Recog. Chem*. **1995**, *21*, 47−78.

22. Jackowski, A.; Zones, S. I.; Hwang, S.-J.; Burton, A. W. Diquaternary Ammonium Compounds in Zeolite Synthesis: Cyclic and Polycyclic N-Heterocycles Connected by Methylene Chains. *J. Am. Chem. Soc.*, **2009**, *131*, 1092−1100.

23. Cox, P. A.; Casci, J. L.; Stevens, A. P. Molecular Modelling of Templated Zeolite Synthesis. *Farad. Discuss*., **1997**, *106*, 473−487.

24. Moliner, M.; Rey, F.; Corma, A. Towards the Rational Design of Efficient Organic Structure-Directing Agents for Zeolite Synthesis. *Angew. Chem., Int. Ed.* **2013**, *52*, 13880–13889.

25. Xie, D.; McCusker, L. B.; Baerlocher, C.; Zones, S. I.; Wan, W.; Zou, X. SSZ-52, a Zeolite with an 18-layer Aluminosilicate Framework Structure Related to that of the DeNOx catalyst Cu-SSZ-13. *J. Am. Chem. Soc*. **2013**, *135*, 10519−10524.

26. Davis, T. M.; Liu, A. T.; Lew, C. M.; Xie, D.; Benin, A. I.; Elomari, S.; Zones, S. I.; Deem, M. W. Computationally-Guided Synthesis of SSZ-52, a Zeolite for Engine Exhaust Clean-up. *Chem. Mater.* **2016**, *28*, 708–711.

27. Broach, R. W.; Greenlay, N.; Jakubczak, P.; Knight, L. M.; Miller, S. R.; Mowat, J. P. S.; Stanczyk, J.; Lewis, G. J. New ABC-6 Net Molecular Sieves ZnAPO-57 and ZnAPO-59: Framework Charge Density-induced Transition from Two- to Three-Dimensional porosity. *Microporous Mesoporous Mater.* **2014**, *189*, 49–63.

28. Castro, M.; Garcia, R.; Warrender, S. J.; Wright, P. A.; Cox, P.A.; Fecant, A.; Mellot-Draznieks C.; Bats, N. Co-Templating and Modelling in the rational synthesis of zeolitic solids. *Chem. Commun.* **2007**, 3470−347.

29. Picone, A. L.; Warrender, S. J.; Slawin, A. M. Z.; Dawson, D. M.; Ashbrook, S. E.; Wright, P. A.; Thompson, S. P.; Gaberova, L.; Llewellyn, P. L.; Moulin, B.; Vimont, A.; Daturi, M.; Park, M. B.; Sung, S. K.; Nam I.-S.; Hong, S. B. A Co-Templating Route to the Synthesis of Cu SAPO STA-7, Giving an Active Catalyst for the Selective Catalytic Reduction of NO. *Microporous Mesoporous Mater*. **2011**, *146*, 36−47.

30. Turrina, A.; Garcia, R.; Cox, P. A.; Casci, J. L.; Wright, P. A. Retrosynthetic Co-Templating Method for the Preparation of Silicoaluminophosphate Molecular Sieves. *Chem. Mater*. **2016**, *28*, 4998–5012.

31. Thompson, S. P.; Parker, J. E.; Potter, J.; Hill, T. P.; Birt, A.; Cobb, T. M.; Yuan, F.; Tang, C. C. Beamline I11 at Diamond: A New Instrument for High Resolution Powder Diffraction. *Rev. Sci. Instrum.* **2009**, *80*, 075107-9.

32. Thompson, S. P.; Parker, J. E.; Marchal, J.; Potter, J.; Birt, A.; Yuan, F.; Fearn, R. D.; Lennie, A. R.; Street, S. R.; Tang, C. C. Fast X-ray Powder Diffraction on I11 at Diamond. *J. Synchr. Radiation* **2011**, *18*, 637–648.

33. Rietveld, H. M. A Profile Refinement Method for Nuclear and Magnetic Structures. *J. Appl. Crystallogr.* **1969**, *2*, 65−71.

34. (a) Larson, A.; von Dreele, R. B. General Structure Analysis System GSAS, Los Alamos National Laboratory, Los Alamos, NM, **2000**. (b) Toby, B. H. EXPGUI, a Graphical User Interface for GSAS. *J. Appl. Crystallogr.* **2001**, *34*, 210−213.

35. Hastings, J. B.; Thomlinson, W.; Cox, D. E. Synchrotron X-ray Powder Diffraction. *J. Appl. Crystallogr.* **1984**, *17*, 85−95.

36. *Materials Studio version 6.1*, Accelrys Inc., San Diego, USA, **2012**.

37. Gale, J. D. GULP: A Computer Program for the Symmetry-Adapted Simulation of Solids. *J. Chem. Soc. Farad. Trans.* **1997**, *93*, 629–637.

38. Sanders, M. J.; Leslie, M.; Catlow, C. R. A. Interatomic Potentials for SiO_2. *J. Chem. Soc. Chem. Commun.* **1984**, *19*, 1271–1273.

39. (a) Rodriguez-Carvajal, J. "FULLPROF: a Program for Rietveld Refinement and Pattern Matching Analysis." *Satellite Meeting on Powder Diffraction of the XV Congress of the IUCr*. Vol. 127. Toulouse, France, 1990; (b) Boultif, A.; Louër, D. Powder Pattern Indexing with the Dichotomy Method. *J. Appl. Cryst.* **2004**, *37*, 724–731.

40. Foster, M. D.; Treacy, M. M. J. *Atlas of Prospective Zeolite Structures.* http://www.hypotheticalzeolites.net/.

41. Mayoral, A.; Sanchez-Sanchez, M.; Alfayate, A.; Perez-Pariente, J.; Diaz, I. Atomic Observations of Microporous Materials Highly Unstable under the Electron Beam: The Cases of Ti-Doped AlPO$_4$-5 and Zn-MOF-74. *ChemCatChem* **2015**, *7*, 3719–3724.

42. Mayoral, A.; Anderson, P. A.; Diaz, I. Zeolites are No Longer a Challenge: Atomic Resolution Data by Aberration-Corrected STEM. *Micron* **2014**, *68*, 146–151.

43. Mayoral, A.; Carey, T.; Anderson, P. A.; Diaz, I. Atomic Resolution Analysis of Porous Solids: A Detailed Study of Silver Ion-Exchanged Zeolite A. *Microporous Mesoporous Mater.* **2013**, *166*, 117–122.

44. Tuel, A.; Lorentz, C.; Gramlich, V.; Baerlocher, Ch. AlPO-ERI, an Aluminophosphate with the ERI Framework Topology: Characterisation and Structure of the As-Made and Calcined Rehydrated Forms. *Comptes Rendus Chimie*, **2005**, *8*, 531–540.

45. Seymour, V. R.; Eschenroeder, E. C. V.; Castro, M.; Wright, P. A.; Ashbrook, S. E. Application of NMR crystallography to the Determination of the Mechanism of Charge Balancing in Organocation-Templated AlPO STA-2. *CrystEngComm* **2013**, *15*, 8668–8679.

46. Blackwell, C. S.; Broach, R. W.; Gatter, M. G.; Holmgren, J. S.; Jan, D.-Y.; Lewis, G. J.; Mezza, B. J.; Mezza, T. M.; Miller, M. A.; Moscoso, J. G.; Patton, R. L.; Rohde, L. M.;

Schoonover, M. W.; Sinkler, W.; Wilson, B. A.; Wilson, S. T. Open-Framework Materials Synthesised in the TMA+/TEA+ Mixed-Template System: The New Low Si/Al Ratio Zeolites UZM-4 and UZM-5. *Angew. Chem. Int. Ed.* **2003**, *42*, 1737–1740.

47. Park, M. B.; Ahn, N. H.; Broach, R. W.; Nicholas, C. P.; Lewis, G. J.; Hong, S. B. Crystallization Mechanism of Zeolite UZS-5. *Chem. Mater*. **2015**, *27*, 1574–1582.

48. Foster, M. D.; Treacy, M. M. J.; Higgins, J. B.; Rivin, I.; Balkovsky, E.; Randall, K. H. A. Systematic Topological Search for the Framework of ZSM-10. *J. Appl. Cryst*. **2005**, *38*, 1028–1030.

49. Mugnaioli, E.; Kolb, U. Applications of Automated Diffraction Tomography (ADT) on Nanocrystalline Porous Materials. *Microporous Mesoporous Mater*. **2013**, *166*, 93–101.

50. Su, J.; Kapara, E.; Liu, L.; Georgieva, V.; Wan, W.; Sun, J.; Valtchev, V.; Hovmöller, S.; Zou, X. Structure Analysis of Zeolites by Rotation Electron Diffraction (RED). *Microporous Mesoporous Mater*. **2014**, *189*, 115–125.